Modifications of astrophysical ices induced by cosmic rays

C. Mejía, A L F de Barros, Alicja Domaracka, P. Boduch, H. Rothard, E. F. da Silveira

A&A, 687, A227 (2024)
https://doi.org/10.1051/0004-6361/202349120

Astronomy & Astrophysics

Modifications of astrophysical ices induced by cosmic rays

I. Water, carbon monoxide, and methanol mixtures

C. Mejía[1], A. L. F. de Barros[2], A. Domaracka[3], P. Boduch[3], H. Rothard[3], and E. F. da Silveira[4]

[1] Facultad de Ciencias Químicas, Universidad de Cuenca, Cuenca 010168, Ecuador
e-mail: cfmejiag@gmail.com
[2] Departament of Physics – CEFET/RJ, Av. Maracanã 229, Rio de Janeiro 20271-110, Brazil
[3] Centre de Recherche sur les Ions, les Matériaux et la Photonique, CIMAP-CIRIL-GANIL, Normandie Université, ENSICAEN, UNICAEN, CEA, CNRS, 14000 Caen, France
[4] Department of Physics, PUC-Rio, Rua Marquês de São Vicente 225, Rio de Janeiro, RJ 22451-900, Brazil

Received 28 December 2023 / Accepted 17 April 2024

ABSTRACT

Aims. Astrophysical ices on dust grain mantles in the interstellar medium (ISM) and dense circumstellar envelopes (CSEs) are continuously exposed to galactic cosmic rays (GCRs). In a laboratory setting, we studied the physical and chemical modifications of ice layers induced by energetic heavy ions as GCR analogues. The ice layers used have a molecular composition similar to that of icy grain mantles.

Methods. Mixtures of H_2O:CO:CH_3OH molecules (percentages 73:24:3, 68:30:3, and 58:38:3) were condensed on a substrate at 15 K and irradiated with 40 MeV $^{58}Ni^{11+}$ ion beams. Irradiation-induced modifications were followed using the mid-infrared absorption spectroscopy technique.

Results. We observed the evolution of infrared bands of CO_2, HCO, HCOOH, CH_4, H_2CO,H_2O_2, and more complex synthesised molecules. From the molecular column densities, cross-sections and sputtering yields were determined and compared to published results of water and carbon monoxide. Analysis of the chemical modifications reveals that the precursors are easily destroyed when they are in a molecular mixture, while others are desorbed.

Conclusions. The main radiolitic modifications induced by GCR irradiations are molecular decomposition and sputtering. Extrapolation to astrophysical radiation conditions shows a strong dependence on the intensity of the GCR distributions at low energies, which allows the analysis of the ice evolution at timescales comparable to those of the ISM and CSE.

Key words. astrochemistry – atomic processes – molecular processes – methods: laboratory: molecular – cosmic rays – ISM: molecules

1. Introduction

Telescopes observing the interstellar medium (ISM) have detected signals of H_2O mixed with molecules such as CO, CO_2, NH_3, and CH_3OH condensed on carbonaceous and silicate dust (Tielens 2013; Boogert et al. 2015). Recent observations performed by the *James Webb* Space Telescope (JWST) have been used to accurately estimate molecular abundances in the ice of dense clouds (McClure et al. 2023). From these measurements, water (H_2O) and carbon monoxide (CO) are found to be the most abundant molecules, followed by carbon dioxide (CO_2) and methanol (CH_3OH), which are possibly synthesised by irradiation (de Barros et al. 2022) via radical–radical reactions or hydrogenation (Chuang et al. 2016). This molecular mixture adheres to interstellar grains and constitutes an ice mantle that is constantly the subject of physical and chemical changes induced by the impact of galactic cosmic rays (GCRs). Replicating the conditions of temperature, pressure, and radiation in the laboratory allows us to understand the physical and chemical modifications induced by the GCR irradiation in the condensed molecules.

Briefly, the combination of H_2O, CO, and CH_3OH molecules in the solid phase has been observed in several regions of the quiescent dense clouds – particularly in their cores – in distinct regions, such as massive, intermediate, and low stellar objects (MYSOs, IMYSOs, and LMYSOs, respectively), in the galactic centre (GC), in comets, and in satellites of the Solar System (Boogert et al. 2015). The percentages of CO and CH_3OH species (with respect to H_2O) are about 12–32% and 2–8%, respectively, in the MYSO, LMYSO, the dense cloud of Taurus, and the quiescent dense clouds of the IC 5146 nebula (Boogert et al. 2015; Chiar et al. 2011; Whittet et al. 2011). H_2O, CO, and CH_3OH molecules were also reported by Bottinelli et al. (2010) in the envelopes of the LMYSOs. In comets, the gaseous abundances of CO and CH_3OH relative to H_2O are 0.4–30% and 0.2–7%, respectively (Mumma & Charnley 2011). In the final section of the present work, the results of the experiment presented here concerning precursor degradation (H_2O:CO:CH_3OH) followed by $H_xC_yO_z$ molecular synthesis are compared with observational findings.

In earlier studies with samples containing hydrogen, carbon, and oxygen (CHO), proton and helium ion beams were used to explore the synthesis of new molecules as well as the implications of the observed modifications to extraterrestrial materials exposed to GCR. Hudson & Moore (1999) identified the products CH_4, HCO, H_2CO, CH_3OH, CO_2, and HCOOH after proton irradiation of H_2O:CO (5:1) samples. Irradiation of samples containing different proportions of H_2O and CO molecules

performed by Ioppolo et al. (2009) and Suhasaria et al. (2017) showed similarities in molecular synthesis with the findings reported by Gerakines et al. (2001). According to Muñoz Caro et al. (2019), the H_2O:CO (4:1) samples irradiated by UV photons generated the same photoproducts as those irradiated by X-rays. Gerakines et al. (2001) found minor variations in the amounts of the synthesised molecules CH_4, CO, HCO, H_2CO, $HCOO^-$, and $C_2H_4(OH)_2$ in an experiment designed to determine differences between the products of H_2O:CO_2:CH_3OH (1:1:1) samples irradiated by UV photons or by protons. Overall, these studies support the notion that molecular syntheses in H_2O:CO samples is probably independent of the irradiation source. However, even though many studies have reported similar chemical and physical modifications of samples under photons or low-energetic light charged-particle irradiation, significant differences caused by swift heavy ion (SHI) irradiation have been observed, such as the highest sputtering yield and high effectiveness of molecular synthesis (Mejía et al. 2022).

In our previous SHI radiolysis experiments, the chemical and physical effects were studied for samples of CO (Duarte et al. 2010), H_2O:CH_3OH (de Barros et al. 2014), H_2O (Mejía et al. 2022), and H_2O:CO (de Barros et al. 2022). These experiments can be used to compare the radiolitic chemical modifications and sputtering yield with previous reports on the molecular mixture H_2O:CO:CH_3OH. The astrochemical purpose of the present study is also to gain further understanding of the influence of energetic heavy-ion cosmic ray irradiation on the evolution of solid samples, and in particular the molecular compositions observed in the ice-mantle of grains in the ISM and dense circumstellar envelopes (CSEs).

2. Experimental

The experiments were performed at the French National Heavy Ion Accelerator (GANIL) IRRadiation SUD (IRRSUD) beamline using the CASIMIR setup of CIMAP-CIRIL ("Centre de recherche sur les Ions, Matériaux et la Photonique"). The CASIMIR system consists of a vacuum chamber (10^{-8} mbar) coupled to a cryostat that allows a CsI substrate to reach the temperature of 15 K (Mejía et al. 2020).

Prior to the experiment, a "blank experiment-type" was performed using the same system without gas deposition. Follow-up examination of the substrate at 15 K showed that residual water gas condensed on both sides of the substrate at a rate of about 8×10^{14} mol h^{-1} cm^{-2}. Thus, the condensation of residual water on one side of the substrate during the experiment (3 h) was approximately 10^{15} mol cm^{-2}, which is less than 0.2% of the initial column density in the sample (Table 1). Other residual gases (CO_2, N_2 and O_2) are expected to adhere to the substrate, but calculations using the chamber's pressure give column densities of less than 1% of the water column density throughout the experiment. Indeed, the molecules condensed on the sample surface are gradually extracted by desorption induced by the SHI irradiation, and the other molecules that adhere to the back of the substrate do not interfere in the radiolytic analysis. Moreover, the column density of the contaminating molecules should increase linearly in time (or fluence), which was not observed.

Ultrapure water (10^7 Ω cm; Milli-Q), carbon monoxide (99.99%, Messer Griesheim), and methanol (99.9%, Aldrich) were introduced into a mixing chamber with a base pressure of 10^{-6} mbar. The desired molecular percentage was prepared via the partial pressure of each gas. To deposit the H_2O:CO:CH_3OH mixture onto the CsI substrate at 15 K, the finger in the setup was adjusted so that the substrate faced the injection tube extremity separated by 10 mm. A valve was then opened to allow condensation of the gas mixture onto the substrate; the residual chamber pressure increased up to 10^{-7} mbar. The deposition time was about 3 min with a deposition rate of almost 10 ± 2 nm s^{-1} and we obtained ice with a thickness of a few micrometres for samples S_1 and S_2, while the deposition rate for the S_3 ice was less than 2 min.

Table 1. Initial and final column densities N_0 and N_f (in 10^{16} molec cm^{-2}) for each of the molecular species that constitute the three samples.

	N_0	N_f	S_e
S_1(73:24:3)			
H_2O	170	146	1183
CO	55.3	8.36	259
CH_3OH	6.84	0.179	97.3
Total	232	154	1540
S_2(68:30:3)			
H_2O	120	96.7	1100
CO	51.6	4.04	333
CH_3OH	4.64	0.064	133
Total	176	100	1566
S_3(58:38:3)			
H_2O	139	114	968
CO	92.5	1.82	481
CH_3OH	8.20	0	141
Total	240	116	1590

Notes. The partial and total electronic stopping powers S_e (in 10^{-15} eV cm^2 mol^{-1}) corresponding to the 40 MeV $^{58}Ni^{11+}$ projectile impinging on each H_2O:CO:CH_3OH sample were computed using the SRIM code (Ziegler et al. 2010).

After restoration of the pressure in the chamber, a valve gate was opened to start the irradiation using the beamline IRRSUD. The $^{58}Ni^{11+}$ ion beam is representative of all the heavy cosmic-ray constituents such as Fe and Si. The nickel abundance in the cosmic-ray distribution is around 2×10^{-4} relative to protons (Tanabashi et al. 2018). The deposited energy is quantified by the electronic stopping power S_{ea} (in 10^{-15} eV cm^2 atm^{-1}) transferred per projectile via electronic interaction with the target and was calculated using the SRIM code (Ziegler et al. 2010); the values for the distinct samples are listed in Table 1. The average electronic stopping power per molecule of each precursor (S_e) is determined by multiplying S_{ea} by the corresponding number of atoms and by their fraction in the sample. For example, for the water in the sample S_1 (73:24:3), S_{ea} is 540 (in 10^{-15} eV cm^2 atm^{-1}), and the electronic stopping power per water molecule is $S_e(H_2O) = S_{ea} \cdot 3 \cdot 0.73 = 1183$ (10^{-15} eV cm^2 mol^{-1}); the same procedure was performed for the other precursors. The total electronic stopping power for the sample S_1 is given by the sum of the three individual electronic stopping powers, $S_e(S_1) = S_e(H_2O) + S_e(CO) + S_e(CH_3OH)$ (see Table 1). The flux of the nickel ion beam impacting the sample surface perpendicularly was roughly 10^9 ion cm^{-2} s^{-1}, which corresponds to the maximum fluence of 10^{13} ion cm^{-2} after the irradiation time of about 167 min. The dose absorbed by the sample for each fluence is calculated as $D = FS_e$, giving a maximum average dose of 16 eV per molecule.

A Nicolet Magna 550 Fourier transform infrared (FTIR) apparatus was used to monitor the ice sample in transmission

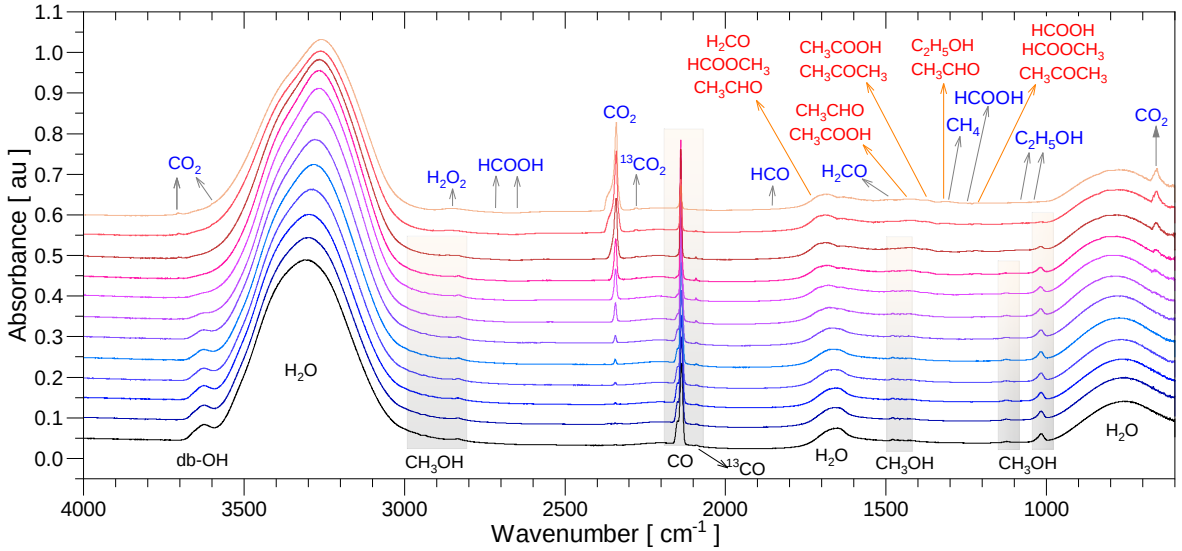

Fig. 1. Infrared spectrum (black bottom line) of non-irradiated ice S_3 (58:38:3) and the IR spectra of the ice for various irradiation fluences. The precursor molecule bands are marked in black, while those corresponding to products appear in blue and red.

mode perpendicular to the sample surface. An infrared (IR) spectrum was recorded for each exposure time after 256 scans with a resolution of 1 cm^{-1} in the 4000–600 cm^{-1} wavelength range. Figure 1 shows the IR spectrum of the sample in absorbance mode, identifying the main IR absorbances of the precursors and products as listed in Tables 2 and 3. We used the Lambert–Beer law (Eq. (1)) to measure the column densities of the precursors or products n, where the integrated absorbance of the i band is $\int_{\nu_1}^{\nu_2} \Lambda_{\rm in}(F)\mathrm{d}\nu$, (in cm^{-1}) and its strength band is the A-value $A_\nu = \Lambda_{\nu \rm in}$, (in cm mol^{-1}).

$$N_n(F) = \ln(10)\frac{\int_{\nu_1}^{\nu_2} A_{\rm in}(F)\mathrm{d}\nu}{\Lambda_{\nu \rm in}}. \quad (1)$$

Equation (1) was used to monitor the precursor and product column densities for each fluence. Although modifications in the molecular composition and structure of the sample during irradiation may affect the absorbance, this equation still provides a good approximation of what occurs in the sample (Mejía et al. 2015b, 2022). The structural evolution of the samples will be addressed in a second paper.

3. Results

The bottom line of Fig. 1 shows the IR spectrum of the H_2O:CO:CH_3OH non-irradiated (58:38:3) sample, as well as the IR spectra for increasing fluence. Spectrum modifications are a consequence of a particular product's synthesis. The following sections address precursor degradation, molecular synthesis, and sample desorption.

3.1. Precursor degradation

The corresponding wavenumbers of the observed IR absorption bands for each precursor molecule in Fig. 1 are presented in Table 2. The analyses of the S_2 and S_3 samples yielded similar results. Four H_2O IR absorptions are identified at 3279, 2200, 1657, and 760 cm^{-1}. The rounded profile of the O-H stretch absorption band at 3279 cm^{-1} confirms the amorphous structure of the ice (Mejía et al. 2015b). Carbon monoxide is identified by the C−O stretch vibrations at 2150 and 2138 cm^{-1}, and the vibrations of its isotopic molecule ^{13}CO at 2100 and 2090 cm^{-1} were also regularly seen in the present experiments. Fourteen methanol IR absorption bands were observed for the three samples; these are reported in Table 2. To compute the H_2O

Table 2. Infrared absorption wavenumber of precursors for the non-irradiated H_2O:CO:CH_3OH ices.

Molecule	ν (cm^{-1})	Identification	A_υ
H_2O	3655	db-OH	–
H_2O	3630	db-OH	–
H_2O	3335	O–H str	20
CH_3OH	2997	C–H	
CH_3OH	2960	C–H str as	
CH_3OH	2935	C–H	
CH_3OH	2915	C–H	
CH_3OH	2834	C–H str s	
CH_3OH	2600	comb	
CH_3OH	2540	comb	
H_2O	2200	comb	
CO	2150	C–O str	
CO	2138	C–O str	1.1
^{13}CO	2100	C–O str	
^{13}CO	2090	C–O str	
H_2O	1650	bend	
CH_3OH	1478	CH_3 def	
CH_3OH	1464	CH_3 def	
CH_3OH	1450	CH_3 def	
CH_3OH	1426	CH_3 def	
CH_3OH	1262	CH_3 def	
CH_3OH	1124	CH_3 rock	1.57
CH_3OH	1017	C–O str	
H_2O	750	lib. wing	

Notes. The A-values ($\times 10^{16}$ cm mol^{-1}) were taken from de Barros et al. (2022). Abbreviations for the IR identification are dangling bonds (db), asymmetric (as), symmetric (s), combination (comb), stretch (str), scissors (scis), bending (bend), deformation (def), libration (lib), winging (wing), and rock (rock).

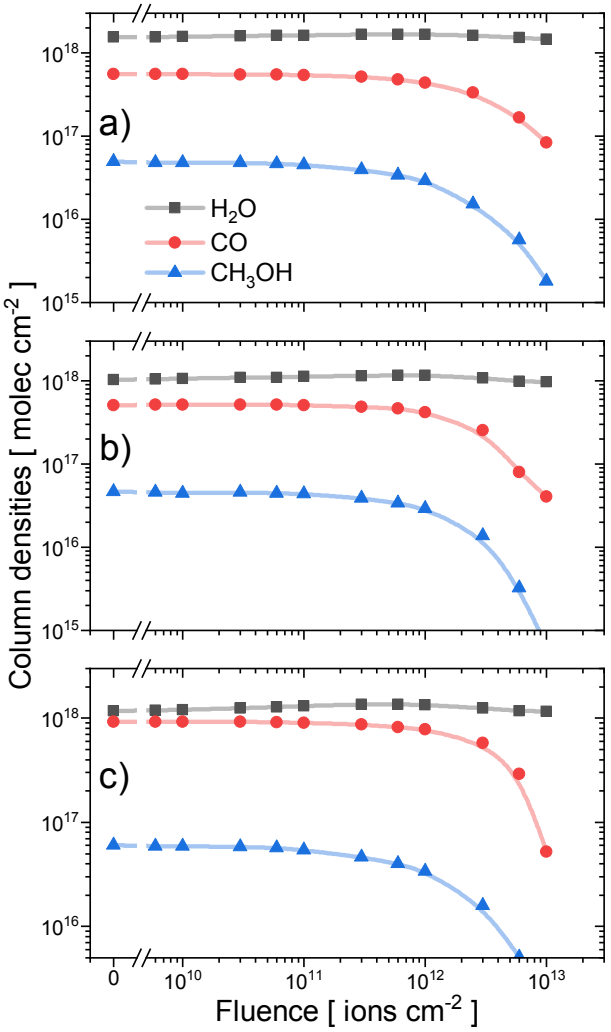

Fig. 2. Precursor column densities as a function of fluence for the following samples: (a) S_1, (b) S_2, and (c) S_3. The lines are the results of fitting Eq. (2).

column density, the absorption around 3200 cm^{-1} was employed, while the infrared region from 2200 to 2100 cm^{-1} for CO and the band 1129 cm^{-1} for CH_3OH were selected because they do not overlap with other IR bands.

Equation (1) – with the respective values of each band strength (Table 2) – was used to monitor the column-density variation of the molecular species during the experiment. Figure 2 presents the column densities of the three precursors as a fluence function. No significant reduction in the H_2O column density was observed for fluences $F<10^{12}$ ions cm^{-2} because the compaction process affects the optical infrared absorption during the irradiation doses of less than 2 eV mol^{-1} (Mejía et al. 2015b), and multiple stretching vibrations of the products rise between 3600 and 3000 cm^{-1} (de Barros et al. 2022). In contrast, as shown in Figs. 1 and 2, the IR bands of CO and CH_3OH and their column densities are weakly affected by the structural changes; also, the IR absorption contributions of the products are minimal.

It is well known from previous studies that SHI irradiation causes physical and chemical modifications in ices (e.g. Mejía et al. 2022). The physical changes generally involve material desorbing from the outermost layers (sputtering). At the same time, the chemical modifications occur as a result of breaks in the bonds of the precursors and the formation of new species in the ion track (molecular synthesis). The degradation of the precursors under irradiation is then determined by the sputtering of the material and the molecular synthesis according to the following equation (Mejía Guamán & Silveira 2013; Mejía et al. 2022):

$$N_k(F) = \left((N_{0k} - N_{\rm csk})\,{\rm e}^{-\sigma_k^{\rm ap}F} + N_{\rm csk}\right) f_{\rm Y}(F), \quad (2)$$

where the apparent or degradation cross-section ($\sigma_k^{\rm ap}$) includes the individual sputtering yield (Y_{0k}) and chemical destruction of the precursor ($\sigma_{\rm dk}$); in turn, these two parameters are balanced by the precursor column density (N_{0k}) by the relation $\sigma_k^{\rm ap} = \sigma_{\rm dk} + Y_{0k}/N_{0k}$ (de Barros et al. 2022). The $N_{\rm csk}$ parameter describes chemical saturation, in which the formation of the precursor from synthesised species at the highest doses balances out the chemical destruction of the precursor. The sputtering yield function $f_{\rm Y}(F)$ describes the material extracted by sputtering yield from the sample surface where $f_{\rm Y}(F) = 1 - \sum Y_{0k}F/N_{0k}$; we note that $f_{\rm Y}(F)$ is close to 1 for low fluences ($F < 10^{12}$ ions cm^{-2}) (Mejía et al. 2022). The $N_{\rm cs}/N_0$ ratio for water molecules is about 0.8, while for carbon monoxide and methanol it is 0. The column density evolution of the sample for low fluences (i.e. $F < 10^{12}$ ions cm^{-2}) in Eq. (2) is approximately linear: $N_k(F) = N_{0k}\left(1 - \sigma_k^{\rm ap}F\right)$. Table 4 presents the precursor's degradation cross-sections obtained by fitting the column-density decrease shown in Fig. 2 with Eq. (2).

3.2. Molecular synthesis

Figure 1 displays the spectrum of the non-irradiated ice mixture and the spectra of the same target irradiated at different fluences. Noteworthy differences between the spectra are observed, particularly the appearance of new IR bands in the spectra after irradiation corresponding to the specific absorptions of molecules synthesised along the projectile path. Although the wavelengths of several new bands coincide or are very close to the wavelengths of some of the precursors, their identification is possible by analysing the IR spectrum evolution as a function of fluence (Fig. 3). Table 3 classifies the observed bands based on literature data.

Figure 3 reveals that the absorption bands of some species are isolated, that is for formic acid HCOOH (2560 cm^{-1}), carbon dioxide CO_2 (2340 cm^{-1}), isotopic carbon dioxide $^{13}CO_2$ (2277 cm^{-1}), formyl radical HCO (1854 cm^{-1}), formaldehyde H_2CO (1497 cm^{-1}), and ethanol C_2H_5OH (1090 cm^{-1}). However, the analysis of the IR bands of HCO, H_2CO and CH_4 (methane) is challenging because the noisy background affects their small absorbances. Although the 2855 cm^{-1} IR band of hydrogen peroxide (H_2O_2) is clearly visible at high fluences (see Fig. 3a), the precise determination of its absorbance is rendered difficult by the presence of the methanol (2834 cm^{-1}) band and by the changes to the baseline of the water OH stretching mode (3335 cm^{-1}).

According to Figs. 3d–f, several IR wavelengths of the formed molecules coincide with the precursor ones. Due to the strong CO stretch vibrations, the region where the most remarkable coincidence occurs is between 1800 and 1500 cm^{-1}. In Fig. 3d, five molecular species with bands around 1700 cm^{-1} may be formed: formaldehyde (H_2CO), formic acid (HCOOH), acetaldehyde (CH_3CHO), methyl formate ($HCOOCH_3$), and acetone (CH_3COCH_3). The locations near 1640, 1600, and 1560 cm^{-1} lack a specific candidate, but these vibrations may possibly correspond to the carbonyl group (Kaiser et al. 2014).

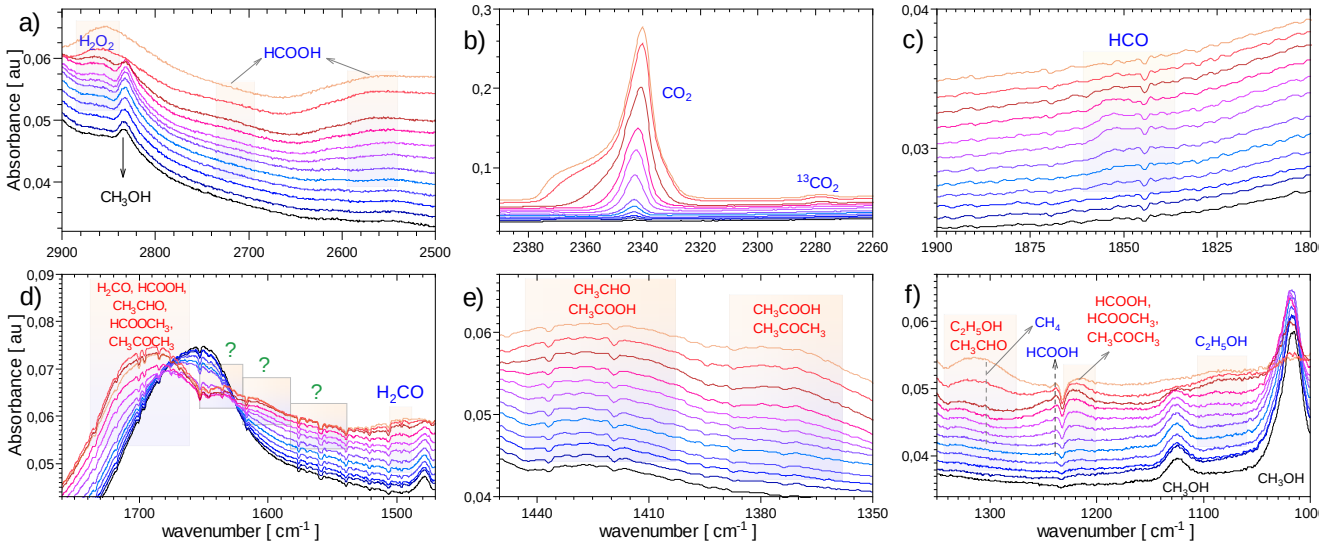

Fig. 3. Infrared absorbances of identified products as a function of fluence for the spectral regions: (a) 2900–2500 cm^{-1} f, (b) 2390–2260 cm^{-1}, (c) 1900–1800 cm^{-1}, (d) 1760–1470 cm^{-1}, (e) 1450–1350 cm^{-1}, and (f) 1350–1000 cm^{-1}.

Table 3. Infrared absorption wavenumber of products after irradiation of 40 MeV $^{58}Ni^{11+}$ for the H_2O:CO:CH_3OH ices.

Molecule	ν (cm^{-1})	Identification	A_v
CO_2	3702	comb	
CO_2	3600	comb	
H_2O_2	2855	O–H str	
HCOOH	2730	O–H, C–H str	
HCOOH	2665	O–H, C–H str	
CO_2	2340	C=O str	7.6
$^{13}CO_2$	2277	C=O str	7.6
HCO	1854		2.1
H_2CO	1718	CO	
$HCOOCH_3$	1718	C=O	
CH_3CHO	1718	C=O str	
HCOOH	1710	C=O str	
CH_3CHO	1710	CO str	
CH_3COCH_3	1710	CO str	
?	1634	C=O str	
?	1609	C=O str	
?	1564	C=O str	
H_2CO	1497	CH_2 scis	0.4
CH_3CHO	1420	CH_3 def	
CH_3COOH	1420	OH bend	
CH_3COOH	1370	CH bend	
CH_3COCH_3	1370	CH_3 def	
C_2H_5OH	1333	OH def	
CH_3CHO	1333	comb	
CH_4	1304	C–H str	
HCOOH	1225	C–O/C–O str	1.5
HCOOH	1222	C–O	
$HCOOCH_3$	1222	C–O	
CH_3COCH_3	1222	CCC str	
C_2H_5OH	1090	CH_3 rock	0.66
C_2H_5OH	1040	CO str	
CO_2	658	CO bend	

Notes. The A-values are based on the results of de Barros et al. (2022). See abbreviations in Table 2.

Other new, multi-contribution absorption bands – shown in Fig. 3e – could likely be associated to acetaldehyde (CH_3CHO) and to acetic acid (CH_3COOH) in the 1445–1400 cm^{-1} region, and acetic acid and acetone in the 1390–1360 cm^{-1} region. From Fig. 3f, the candidate molecular species with bands around the 1300 cm^{-1} absorption are C_2H_5OH and CH_3CHO, while around 1222 cm^{-1} the candidate species are HCOOH, $HCOOCH_3$, and CH_3COCH_3.

For the single absorption bands that can be followed during irradiation, their corresponding column densities can be calculated using Eq. (1). The selected molecules are CO_2 (at 2341 cm^{-1}), HCO (at 1850 cm^{-1}), and C_2H_5OH (at 1090 cm^{-1}), and the evolution of their column densities is shown in Fig. 4. As proposed by Mejía Guamán & Silveira (2013), and Mejía et al. (2022), the evolution of the product column densities can be described by

$$N_j(F) = \frac{\sigma_{fj}}{\sigma_{dj}} \left(1 - e^{-\sigma_{dj} F}\right) f_Y(F) \sum_{k=1}^{3} N_{0k}, \quad (3)$$

where σ_{fj} and σ_{dj} are the formation and destruction cross-sections of the j species; the sum includes the column densities of the three precursors. Assuming the sputtering yield function approximation $f_Y(F) \approx 1$ for $F < 10^{12}$ ions cm^{-2}, the cross-sections obtained by fitting Eq. (3) are shown in Table 4.

4. Discussion

4.1. Precursor degradation

Much of the previous research on the destruction cross-section of a single precursor as a function of S_e^n has focused on finding the value of power n, which was found to fall within the ranges $1 \leq n \leq 1.5$ (e.g. de Barros et al. 2011; Mejía et al. 2015a, 2022). One major drawback of the approach to finding the value of S_e is that the limitations of the code SRIM (Ziegler et al. 2010) are such that the diverse ways in which the ion–solid interaction releases energy into the electronic system are indistinguishable, and the chemical processes triggered by the electronic interaction are omitted. Notwithstanding these disadvantages, we used

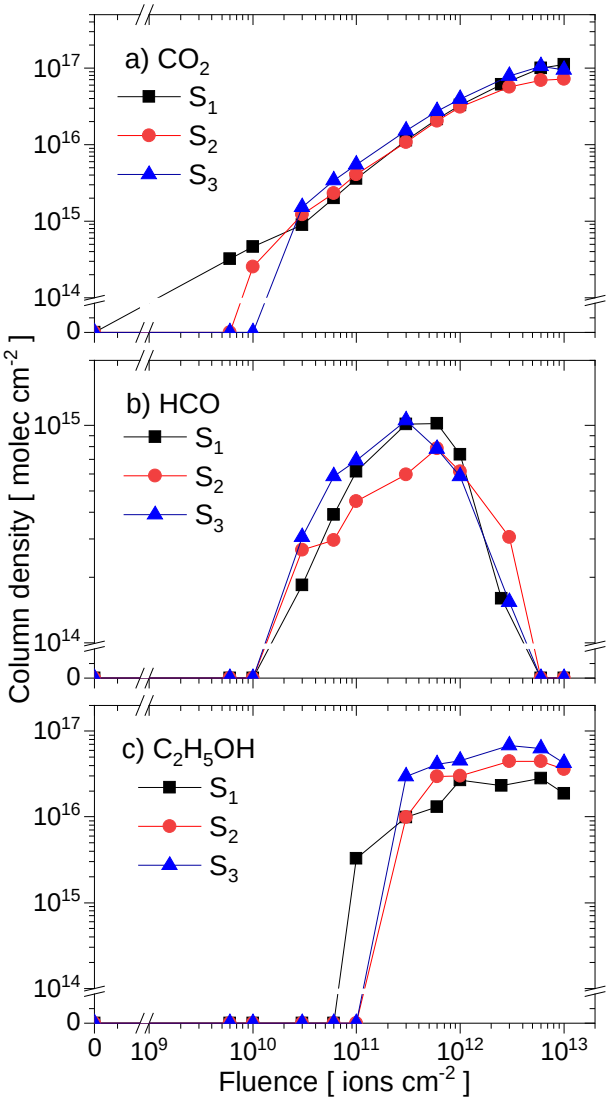

Fig. 4. Product column densities as a function of fluence for (a) CO_2, (b) HCO, and (c) C_2H_5OH.

the value of S_e computed by the SRIM algorithm to assess the physical and chemical modifications proposed in the previous analysis.

As explained in Sect. 3.1, the breaking of chemical bonds – quantified by σ_d – and the desorption of material – quantified by Y_0 – are responsible for the degradation of precursors σ^{ap}, but this process also depends on N_0. Thus, these two contributions, expressed together via the equation $\sigma^{ap} = \sigma_d + Y_0/N_0$, restrict the calculation of each parameter, making it difficult to measure the contribution of chemical and physical changes and making it even more hard to interpret these changes when there are various precursors at different concentrations. Despite this problem, as a benchmark, each precursor's degradation cross-section (Table 4) may be better understood by comparing it to the degradation cross-sections of irradiated pure samples, considering the different values of electronic stopping power (Fig. 5).

Figure 5 displays the apparent (or degradation) cross-section dependence on the electronic stopping power of the CH_3OH, CO, and H_2O precursors for two conditions: (i) individually, when samples consist of a unique precursor (corresponding to the fitting line), and (ii) for ice mixtures (scattered data).

Table 4. Formation and destruction cross-section (in 10^{-14} cm^{-2}) of products and precursors for the irradiated H_2O:CO:CH_3OH ices with 40 MeV $^{58}Ni^{11+}$ ions.

	S_1	S_2	S_3
Formation	(73:24:3)	(68:30:3)	(58:38:3)
HCO	0.36 ± 0.08	0.40 ± 0.10	0.48 ± 0.10
CO_2	1.61 ± 0.13	2.28 ± 0.25	2.46 ± 0.28
C_2H_5OH	1.8 ± 0.4	3.1 ± 0.5	3.5 ± 0.5
Destruction			
HCO	790 ± 100	1054 ± 320	1420 ± 450
CO_2	31.1 ± 1.0	55.4 ± 2.0	51.4 ± 2.0
C_2H_5OH	155 ± 45	120 ± 30	143 ± 40
H_2O	13 ± 3	20 ± 8	27 ± 4
CO	22 ± 2	21 ± 1	19 ± 1
CH_3OH	57 ± 14	45 ± 14	68 ± 12

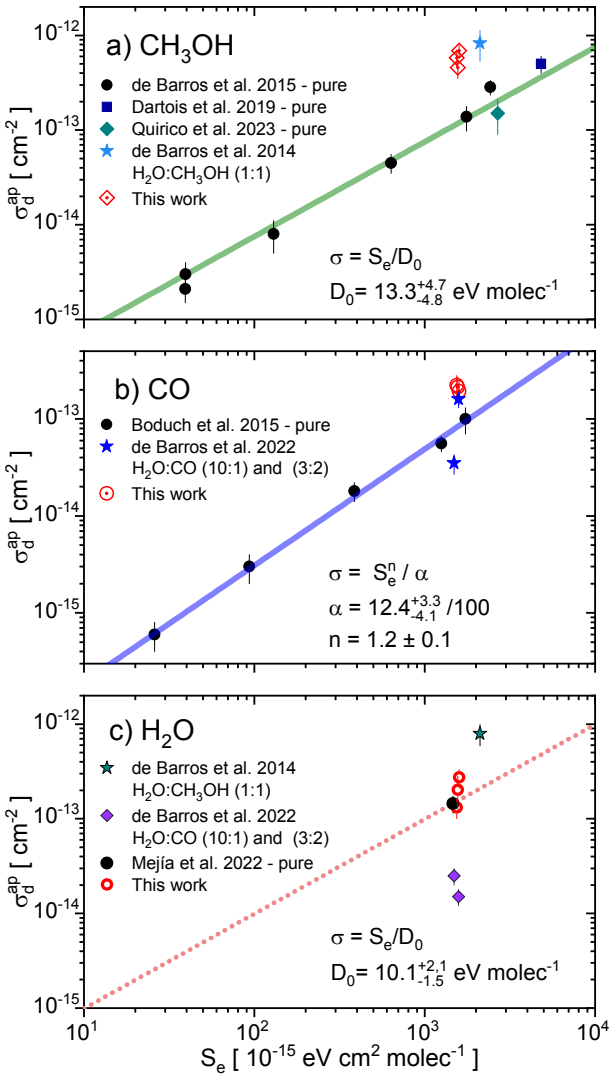

Fig. 5. Apparent destruction cross-sections of precursors as a function of the electronic stopping power for (a) CH_3OH (de Barros et al. 2011, 2014; Dartois et al. 2019; Quirico et al. 2023), (b) CO (Boduch et al. 2015; de Barros et al. 2022), and (c) H_2O (de Barros et al. 2014, 2022; Mejía et al. 2022).

Figure 5a reveals a linear relationship between the destruction cross-section of pure methanol and S_e (de Barros et al. 2011; Dartois et al. 2019; Quirico et al. 2023). We note that for the CH_3OH degradation in the H_2O:CH_3OH (1:1) mixture, de Barros et al. (2014) found relatively high CH_3OH destruction cross-sections; the results presented here follow a similar behaviour for the precursor CH_3OH in the presence of H_2O and CO. Upon inspection of the data in Table 4, we find that the destruction cross-sections of the CH_3OH molecule are higher than those of the H_2O and CO precursors. It is conceivable that the chemical destruction of CH_3OH is intensified because radical fragments of H_2O and/or CO species promote chemical reactions that lead to the synthesis of complex molecules.

Figure 5b shows the apparent destruction cross-section as a function of S_e for pure CO and CO:H_2O. Boduch et al. (2015) reported that for pure CO ice, this dependence is $\sigma^{ap} = S_e^{1.2}/\alpha$. Data for CO in the mixture of H_2O:CO ice for the (3:2) and (10:1) concentrations are adapted from de Barros et al. (2022). The ratio between the destruction cross-sections for these two concentrations is $\sigma(3{:}2)/\sigma(10{:}1) \approx 4.5$, demonstrating that the CO molecule is more radioresistant at the highest H_2O concentration. For the three sample concentrations used in the current experiment, the CO destruction cross-section for SHI irradiation is roughly 2×10^{-13} cm^{-2}, which is twice that expected above the reference line for pure carbon monoxide destruction. This is likely due to the high concentration of radicals that effectively react with surrounding species to synthesise new molecules in the ion track (Mejía et al. 2020).

The dependence of the apparent destruction cross-section of H_2O on S_e is displayed in Fig. 5c. Cross-sections for low stopping powers are sparse in the literature because structural changes affect the IR absorption bands for low irradiation doses, preventing column density measurements (Mejía et al. 2015b). Nevertheless, Mejía et al. (2022) reported the chemical destruction cross-section for pure amorphous water for high irradiation doses even for lower values of S_e as $\sigma = S_e/D_0$, with $D_0 \approx 10^{+2.1}_{-1.5}$ eV mol^{-1}. Starting from this result, the dashed line in Fig. 5c refers to the destruction cross-sections of water in the presence of other species.

By comparing the destruction rates displayed in Fig. 5, the H_2O molecule degrades about 40 times faster in the H_2O:CH_3OH (1:1) ice than in ices composed of H_2O:CO (3:2 and 10:1) (de Barros et al. 2014, 2022). Moreover, H_2O degrades slower when CO is present in the H_2O:CO ices. The presence of CH_3OH species in the H_2O:CO:CH_3OH ice seems to balance the high level of destruction of H_2O in the H_2O:CH_3OH ice with the low destruction of H_2O in the H_2O:CO ice for an intermediate rate of destruction. Table 4 highlights that the destruction of the H_2O molecule for each sample is the highest when the CH_3OH concentration is also the highest.

4.2. Sputtering of molecules from the sample surface

As described in Sect. 3.1, the precursor degradation is given by $\sigma_k^{ap} = \sigma_{kd} + Y_{0k}/N_{0k}$. The calculation of the sputtering yield is well established: it depends on the square of the stopping power. Indeed, for pure molecular samples, Duarte et al. (2010) demonstrated that the relationship $Y_{CO} = S_e^2/21.6$ holds for pure CO; from previous reports, Mejía et al. (2022) confirmed the square power law $Y_{H_2O} = S_e^2/340$ for pure H_2O (for $T < 80$ K); and Dartois et al. (2019) stated that the sputtering yield for CH_3OH may be approximated by the relation $Y_{CH_3OH} = S_e^2/1160$. Using these relationships to estimate the sputtering yields of each molecule in a pure sample irradiated by the 40 MeV $^{58}Ni^{11+}$ ion projectile, one gets $Y_{H_2O} = 6.2 \times 10^3$, $Y_{CO} = 1.3 \times 10^5$, and $Y_{CH_3OH} \approx 6.6 \times 10^3$ molecules per ion for H_2O, CO, and CH_3OH, respectively. The water and methanol sputtering yields are comparable, but the value for carbon monoxide is almost 20 times higher. This difference suggests that the total sputtering yield of the H_2O:CO:CH_3OH mixture is mainly reduced by the presence of water and not by the carbon monoxide component. In addition, the high values of Y_{CO} enhance the CO apparent destruction cross-section (which includes the sputtering), increasing the S_e power n from 1 to 1.2 (see Fig. 5b).

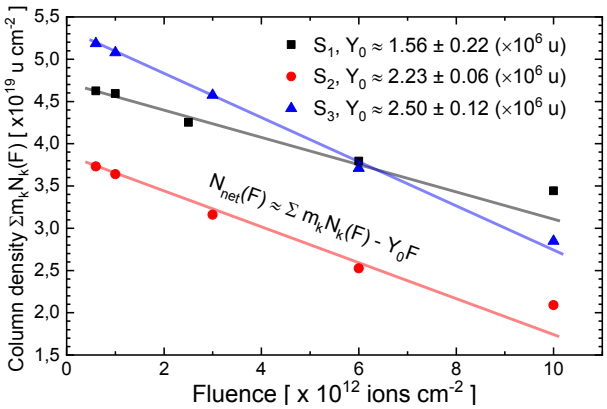

Fig. 6. Fitting of column densities using Eq. (6) for the three samples. The slope of the lines is approximated as Y_0.

To first approximation, the predicted sputtering yield (Y_{sp}) of a composed material is described by a combination of all independent molecular sputtering yields expressed in atomic mass units per ion (u ion^{-1}) for each species in the irradiated sample:

$$Y_{sp} = \sum_{k=1}^{n} m_k c_k Y_k, \tag{4}$$

where for each k molecular species, m_k is the molecular mass, c_k is the abundance fraction, and Y_k the sputtering yield. Neglecting the sputtering of products (usually with an abundance fraction much lower than the precursors), the sample sputtering yield for the studied ice mixture is:

$$Y_{sp} \approx 18 c_1 Y_{H_2O} + 28 c_2 Y_{CO} + 32 c_3 Y_{CH_3OH}. \tag{5}$$

For the H_2O:CO:CH_3OH sample irradiated with a 40 MeV $^{58}Ni^{11+}$ ion beam, the approximated values of Y_{sp} are 0.96, 1.2, and 1.5 ($\times 10^6$ u ion^{-1}) for S_1, S_2, and S_3, respectively.

Mejía et al. (2020) showed that the net sputtering yield of mixed molecular samples can be approximated by the evolution of the total material in the sample during irradiation by

$$N_{net}(F) \approx \sum_{1}^{k} m_k N_k(F) - Y_{net} F, \tag{6}$$

where $N_{net}(F)$ is the number of atoms (in atomic units) and Y_{net} is the net sputtering material. This expression disregards the condensation of the residual gases in the vacuum chamber. After fitting data using Eq. (6) (see Fig. 6), the sputtered masses per impact for the S_1, S_2, and S_3 samples are 1.5, 2.2, and 2.5 (± 0.2 times 10^6 u ion^{-1}), respectively. The material sputtered from the sample surface should be less because unobserved species have not been included in Eq. (6). Also, the effects due

to molecular forces between the precursor and product molecules have not been included.

These outcomes corroborate those of de Barros et al. (2022), who also found that the net sputtering yield for H_2O:CO samples (for concentrations of 3:2 and 10:1) was about 2×10^6 u ion^{-1}, a value reasonably close to that determined using Eq. (5). Comparing the calculations of Eqs. (5) and (6), the 'real' sputtering yield ($Y_{\rm real}$) should be an intermediate value: $Y_{\rm sp} < Y_{\rm real} < Y_{\rm net}$ (i.e. $10^6 < Y_{\rm real} < 2.5 \times 10^6$ u per ion). These results neglect the influence of other factors on the sputtered material approximations, such as sample structure and intermolecular forces. Further experiments that take these factors into account could shed more light on the sputtering yields of mixture molecular ice samples.

4.3. Molecular synthesis

The inelastic interaction between the projectiles and the sample triggers several energetic processes: ionisation, excitation, and fragmentation of the precursors along the path throughout the projectile track. Products may react chemically with each other or with intact precursors to synthesise new chemical species. New vibrations, corresponding to formed molecular species, are observed in the IR spectra, as shown in Figs. 1 and 3. The evolution of the column density of the products CO_2, HCO, and C_2H_5OH is shown in Fig. 4.

The CO_2 column density shows the same behaviour for the three irradiated samples. The column density of carbon dioxide increases up to the fluence of 6×10^{12} ion cm^{-2}, where possibly the chemical equilibrium is reached (Mejía et al. 2022). The CO_2 molecule comes from the irradiated sample and not from condensed residual gases of the vacuum chamber; otherwise, its column density should increase steadily. It is important to note that the CO_2 abundance is related to the abundance of oxygen and carbon present in the sample, and it is one of the molecules readily synthesised in samples containing the CHO elements (de Barros et al. 2014, 2022).

What stands out most about the evolution of HCO abundances is that, after being synthesised, its band (1884 cm^{-1}) disappears from the spectra for fluences above 6×10^{12} ion cm^{-2} (see Fig. 4b). This behaviour has been observed by other authors, such as Dartois et al. (2019). The HCO radical could be formed in the outermost layers, where the hydrogen concentration is scarce owing to its sublimation, and HCO molecules can be easily desorbed from the surface by continuous sputtering during irradiation (Mejía et al. 2020). However, the rapid disappearance of the HCO radical could also be attributed to chemical reactions with other species in the bulk.

Ethanol formation has already been observed in irradiated samples, such as mixtures of water with methanol (de Barros et al. 2014), water with methane (Mejía et al. 2020), and water with carbon monoxide (de Barros et al. 2022). This finding is remarkable because CH_3CH_2OH has a more complex chemical structure with respect to its precursors and has a probable connection to the disappearance of the HCO molecule. Figure 4c shows that ethanol becomes visible at the fluence of $F = 2 \times 10^{12}$ ion cm^{-2}, increases up to 4×10^{12} ion cm^{-2}, and then starts to decrease slightly, whereas the formyl radical shows a marked decrease at the same fluences (Fig. 4b). Thus, the disappearance of the HCO molecules may have contributed to the synthesis of the C_2H_5OH species. Nevertheless, the synthesis of C_2H_5OH may involve numerous complex chemical pathways, including molecules distinct from HCO (Bergantini et al. 2018).

The likely formation of molecules with a more complex structure than their precursors, such as $HCOOCH_3$, CH_3CHO, CH_3COOH, and CH_3COCH_3, is an interesting result. These molecules have been reported in previous experiments with water-rich ices by Bennett et al. (2005), Bennett & Kaiser (2007), and Mejía et al. (2020). The inherent limitations of the FTIR apparatus (i.e. low resolution and range) and the technique used to analyse the irradiated samples prevent quantification and unambiguous confirmation of the presence of these compounds.

5. Astrophysical implications

In this section, the cross-sections and sputtering measurements presented in Sects. 3.1, 4.1, and 4.2 are applied to the astrophysical conditions of mantle ice on grains under the action of GCRs. The following procedure is employed to achieve this (see e.g. Mejía et al. 2022). The astrochemical ionisation or sputtering rates induced by GCRs are estimated by integrating the dissociation rate over the GCR abundance and energy distributions,

$$H_{rGCR}(r, \alpha, E_0) = \sum_z \iiint R_{rz}(r, E)\Phi_z(\alpha, E, E_0)\, {\rm d}E\, {\rm d}\Omega. \quad (7)$$

For isotropic radiations, the integral of the solid angle is $\int {\rm d}\Omega = 4\pi$. The experimental radiolitic rate (connected to cross-sections or sputtering yield) is represented by $R_{rz}(r, E)$ as a function of the ion energy per nucleon E of the z element (z = H, He, C, O, Ne, Mg, Si, S, Ar, Ca, Fe, and Ni) (Maurin et al. 2014). The GCR distribution is described by the analytical expression

$$\Phi_z(\alpha, E, E_0) = C_z \frac{E^\alpha}{(E + E_0)^{2.7+\alpha}}, \quad (8)$$

where the constant C_z represents the abundance of the z element, while the parameter α can take distinct values based on observations and approximations of $\Phi_z(\alpha, E, E_0)$. The model studied by Shen et al. (2004) uses $\alpha = 0.3$, and we refer to this as model $\mathscr{S}$. Ivlev et al. (2015) suggested two models $\alpha = 0.1$ (model $\mathscr{L}$) and $\alpha = -0.8$ (model $\mathscr{H}$). Measurements performed by the Voyager 1 spacecraft in the local ISM give $\alpha \approx 0.26$ for lower energies of protons (model $\mathscr{V}$) (Cummings et al. 2016). These distributions were adopted to obtain further in-depth information on the GCR rates in different conditions where GCRs can be attenuated, deflected, and implanted in molecular clouds, and/or altered by magnetic fields (Padovani et al. 2018). The interaction of GCRs with matter and magnetic fields could be reflected in the variation of the parameters C_z, α, and E_0 (Maurin et al. 2014; Cummings et al. 2016).

The parameter E_0 regulates the GCR distribution for low energies $E < E_0$, assuming typical values of between 100 and 2000 MeV per nucleon. The astrochemical rate $H_{rGCR}(r, \alpha, E_0)$ is therefore a function of the parameters E_0, C_z, and α, and depends on the rate function $R_{rz}(r, E)$ selected as a function of the experimental radiochemical constant r (e.g. D_d or ψ). In the sections below, the chemical modifications and sputtering yield are described via the $H_{\rm rGCR}(r, \alpha, E_0)$ function.

5.1. Radiochemical dissociation rates

The absorbed dose by the sample is $D = FS_{\rm e}$ which, adapted to Eq. (7), is written as $R_{{\rm dose}-z}(E) = S_{ez}(E)$; the fluence is substituted by the $\Phi_z(\alpha, E, E_0)$ function for a specific value of E_0 and α. Then, after numerical integration of Eq. (7) in the energy

Table 5. Exponents of GCR distribution models of Eq. (8). Parameters for the GCR rates of Eqs. (9), (10), and (12).

Model	α	β	log λ	γ	log κ
$\mathscr{S}$	0.3	2.33	–7.75	2.76	10.30
$\mathscr{V}$	0.26	2.33	–8.05	2.76	10.2
$\mathscr{L}$	0.1	2.33	–7.52	2.64	10.62
$\mathscr{H}$	–0.8	1.88	–6.75	1.88	10.61

range from 10^{-5} to 10^{4} MeV per nucleon, the absorbed dose for each value of E_0 and α is obtained:

$$D_{\rm GCR}(t, E_0) = \frac{\lambda t}{E_0^{\beta}}, \tag{9}$$

where the values of λ (in units of eV mol^{-1} s^{-1} (MeV /u)$^{\beta}$) and β for each GCR distribution model are listed in Table 5. Figure 7 displays the chemical modification region for doses of lower than 10 eV mol^{-1} and their equivalent times for various values of E_0. For the precursor degradation, the dissociation cross-section can be assumed – to a good approximation (Mejía et al. 2015b) – to be proportional to the electronic stopping power, $\sigma_{dk} = S_e/D_{0k}$ (see Sect. 4.1). Then, to obtain the dissociation rate $H_{\rm dGCR}$, the $R_{\rm dz}(E)$ is replaced by S_e/D_{0k} in Eq. (7). The values of D_{0k} are obtained from Fig. 5 for CH_3OH→2.2 eV mol^{-1}, CO→7 eV mol^{-1}, and H_2O→8 eV mol^{-1}.

$$\xi_{dk}(D_{0k}, E_0) = \frac{\lambda}{D_{0k} E_0^{\beta}}. \tag{10}$$

All values of $\xi_{\rm d}(E_0)$ for water as a precursor for the GCR models of Table 5 are shown in Fig. 8. The half lifetime for ionising the precursor k is written $\tau_{dk1/2} = \ln(2)/\xi_{dk}(D_{0k}, E_0)$. On the other hand, the chemical saturation observed in Fig. 4 occurs at a dose of around 10 eV mol^{-1}. At this absorbed dose, the timescale of the GCR irradiation also depends on the parameter E_0. For example, using Eq. (9) for 200 MeV nucleon^{-1} for the $\mathscr{S}$ model, the chemical equilibrium is reached in $t_{\rm cs} = 10E_0^{2.33}/\lambda \approx 4$ Myr. The ionisation parameter ξ_{dk} ($\mathscr{S}$ model) for the water precursor is slightly higher than those for pure water reported by Mejía et al. (2022). Consequently, the chemical dissociation rates of precursors increase for both decreasing water concentration and decreasing GCR intensity for energies $E < E_0$. These results indicate that icy mantles with higher water concentrations have a longer lifespan. This proposition may be confirmed by future observations conducted by the JWST.

5.2. Sputtering rates

Following the procedure proposed by Mejía et al. (2022), the sputtering yield rate induced by cosmic-ray irradiation can be calculated as

$$\eta_(\psi, E_0) = 2 \sum_z \int 4\pi Y_z(\psi, E) \Phi_z(\alpha, E, E_0)\, {\rm d}E, \tag{11}$$

where $Y_z(\psi, E) = S_{ez}^2(E)/\psi^2$ (with $\psi \approx 2$ eV mol^{-1} 10^{-15} cm^2). The factor 2 in Eq. (11) assumes that the GCR traverses the grain. Then, the sputtering rate triggered by GCR irradiation is written as

$$\eta_(\psi, E_0) = \frac{\kappa}{\psi^2 E_0^{\gamma}}. \tag{12}$$

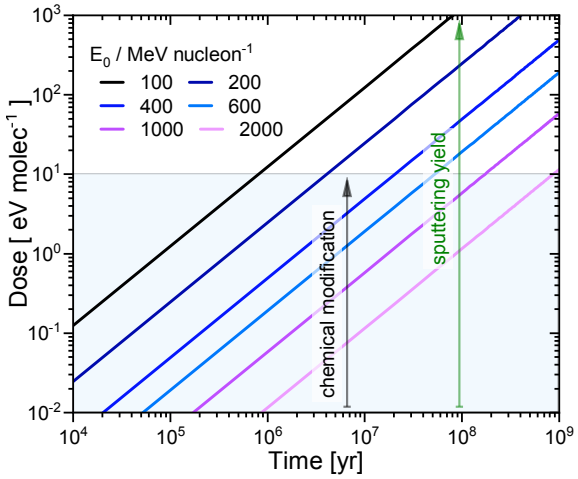

Fig. 7. GCR irradiation dose for the $\mathscr{S}$ model as a function of time for values of the E_0 parameter in the 100–2000 MeV u^{-1} range (see Eq. (9)). The shaded areas indicate the extent to which chemical changes occur ($D < 10$ eV mol^{-1}).

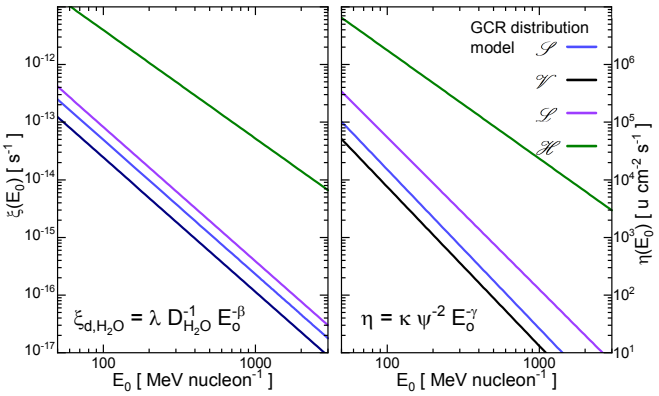

Fig. 8. GCR rates for different distribution models of Table 5 as a function of the E_0 parameter; see Eqs. (10) and (12). The left axis corresponds to the water precursor dissociation rate, while the right axis represents the sputtering yield rate.

For the $\mathscr{S}$ and $\mathscr{V}$ models, the constant κ varies in the range $10^{10} < \kappa < 2 \times 10^{10}$ (u cm^{-2} s^{-1} (eV mol^{-1} 10^{-15} cm^2)^2 (MeV u^{-1})$^{\gamma}$), once the calculated sputtering yield in Sect. 4.2 is in the range of $10^6 < Y_{\rm real} < 2.5 \times 10^6$ u per ion for the three samples. As shown in Fig. 8, the possible values of $\eta_(E_0)$ (right side) are plotted as a function of the E_0 for the four GCR distribution models presented in Table 5. The function $\eta_(E_0)$ for the $\mathscr{H}$ model exhibits the highest values compared to the other models because their GCR distribution is higher at energies of lower than 100 MeV (Ivlev et al. 2015).

As previously mentioned, the desorption yield for the mixed sample is much higher than that for pure water. This difference should also be seen for the grain mantles, and this can be illustrated briefly by considering that a fraction of the total sputtering rate corresponds to water molecules. For example, the fraction of water molecules desorbed may be 50%, which is $\eta_{\rm H_2O}(E_0) \approx 0.5\eta(E_0)/18$. Comparing $\eta_{\rm GCR}(E_0)$ with those reported by Mejía et al. (2022) for pure water ice, the water sputtering yield for a mixed sample can be about 80 to 160 times higher. This comparison suggests that the material desorbed from the ice mantle of grains in the ISM and CSE is most probably determined by the carbon monoxide component in the ice, because this molecule

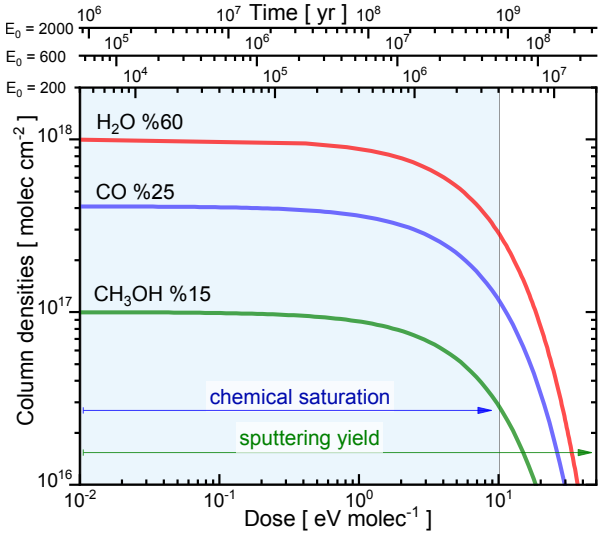

Fig. 9. Column densities of precursors as a dose function for the $\mathscr{S}$ and $\mathscr{V}$ models for the sample proportion H_2O:CO:CH_3OH (60:25:15). The chemical modifications cease when $D \leq 10$ eV mol^{-1}; while the sputtering yield is continuous over the GCR irradiation. The timescales for values of 200, 600, and 2000 MeV u^{-1} are shown at the top.

significantly increases the amount of material sputtered from the mixed molecular sample (see Sect. 4.2). This valuable result may be used in astrochemical models to better understand the desorption of interstellar matter from ice mantles. It should also be compared with that induced by other types of ionising radiation, such as electrons and photons, in order to estimate a realistic desorption rate from the grain surfaces.

The regions where the degradation of the precursor should probably occur and the sputtering yield are presented in Fig. 9. This figure represents the mantle ice evolution in the local ISM under GCR irradiation, where Voyager 1 is likely to observe. The precursor column densities for a hypothetical ice composition H_2O:CO:CH_3OH (60:25:15) as a dose and time function are calculated, replacing the GCR rates (ξ_{dk} and η) of the $\mathscr{S}$ model in Eqs. (2) and (3). The chemical modifications cease at doses close to 10 eV mol^{-1}. On the other hand, sputtering is uninterrupted during the GCR irradiation. It can therefore be assumed that the sputtering rate generated by GCR is the main factor in the degradation of the ice mantle of interstellar grains. In addition, the GCR timescales are compared for the different values of E_0. The results of this comparison undoubtedly demonstrate that the evolution of ice depends on the intensity of cosmic rays at energies $E < E_0$. As opposed to what is suggested by the representation shown in Fig. 9, the attenuation of GCRs cannot be omitted as they pass through the column density of hydrogen clouds ($\sim 10^{22}$ mol cm^{-2}) until they reach the gases condensed on the cold grains (Padovani et al. 2018). This attenuation in the intensity of GCR distribution affects low-energy elements, and consequently the dissociation and sputtering constants (Table 5) may decrease by an order of magnitude.

5.3. Molecular composition compared with observations

Currently, the JWST carries out much more precise IR observations than its predecessors. The infrared spectra already acquired for the cold regions of the ISM and the circumstellar regions reveal a vast diversity of complex molecules containing mainly CHON elements (Boogert et al. 2015). As a result, the molecular composition of the dense cloud ice was measured in the direction of the two background stars NIR38 and the so-called J110621 (McClure et al. 2023). These molecular abundances have been compared with the recorded abundances found in comets (Mumma & Charnley 2011); in the spectra of the icy mantles towards the star Elias 16 behind the Taurus and Serpens molecular clouds (Knez et al. 2005); in high-, intermediate-, and low-massive young stellar objects (MYSOs, IYSOs, and LYSOs) (Boogert et al. 2015); in the interstellar environment of quiescent regions; and in the central and outer galaxies. Here, we compare these molecular abundances observed by telescopes with the experimental molecular abundances measured by de Barros et al. (2022) and the results of this work after an average dose of nearly 6 eV per molecule.

The barplot shown in Fig. 10 reveals one of the most marked discrepancies between the measured molecular percentages of the ice mantle and these percentages derived here. Our experiments yielded lower values for each molecule, but a few possible explanations exist for this difference. Concerning the sample analysed in the laboratory, either the initial precursor concentration used to simulate the composition of the ice mantles was incorrect, or another precursor is lacking. Regarding the latter case, the composition of an ice mantle includes abundant carbon dioxide and ammonium (Boogert et al. 2015), and realistic experiments must include these as precursors. Another possible explanation is that molecules constantly condense on the surface of the cold grain, according to a recent report by Perotti et al. (2020).

Due to various phenomena such as molecular condensation, desorption, and chemical reactions on the grain surface, the chemical composition of a sample processed with ionising radiation may not accurately simulate the frozen mantle. Future experiments are required to assess the incorporation of other molecular precursors, which will help us better understand the physical and chemical evolution of icy grain mantles.

6. Conclusions

This investigation was carried out to examine the physical and chemical modifications induced by energetic ion irradiation of an ice mixture containing H_2O, CO, and CH_3OH , which is analogous to astrophysical ice molecular species detected in the ISM and CSE. We quantified the degradation of precursors, molecular synthesis, and sputtering yields. Our main findings can be summarised as follows:

1. In the present study we assessed the degradation of the precursors based on results taken from the literature (Fig. 5). Using the relationship $\sigma_{dk} \approx S_e/D_{0k}$ for irradiated pure ices, we find that the CO and CH_3OH molecules are more efficiently destroyed when present in small percentages relative to water. Furthermore, H_2O is more easily degraded by radiolysis in the mixture when compared to its degradation in pure water. Prior to this study, it was hard to measure precursor degradation because there was no benchmark against which to evaluate this process for samples containing multiple precursors.
2. These findings enhance our comprehension of precursor degradation and sputtering. From the analysis in Sect. 4.2, we infer that the real sputtering yield (Y_{real}) lays between the individual sputtering yield (Y_{sp}) of each precursor and the estimated net sputtering yield (Y_{net}) calculated from the observable molecular species evolution. Indeed, the real sputtering yield for the three samples is measured in the range of $10^6 < Y_{real} < 2.5 \times 10^6$ u per incoming projectile.

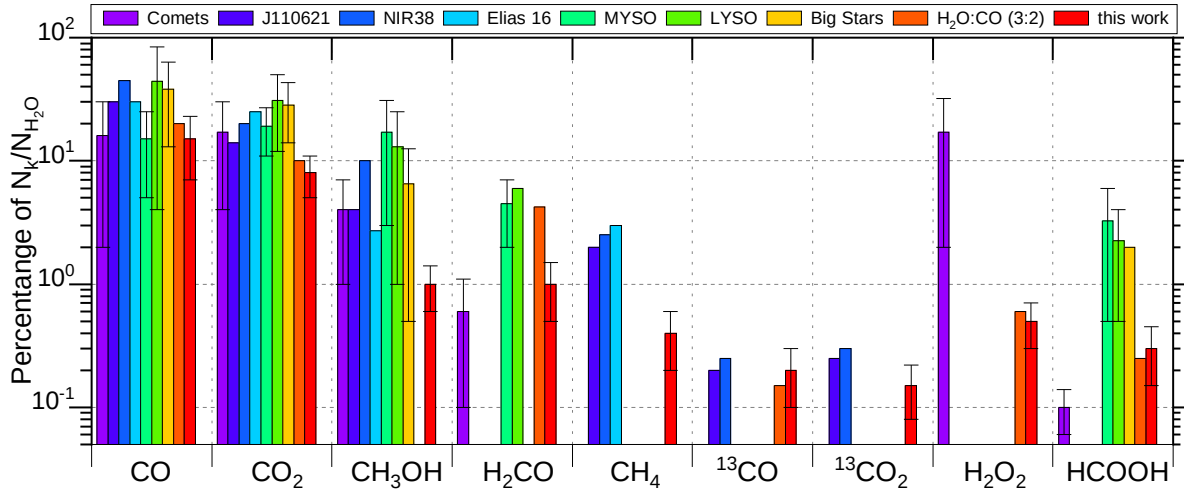

Fig. 10. Barplot of molecular percentage with respect to water for species containing the CHO elements. Percentage of molecules observed in comets (Mumma & Charnley 2011). From the J110621 and NIR38 regions detected by the JWST by McClure et al. (2023). Molecules identified in MYSO, LYSO and Big Stars (see text for details), average percentages were adapted from Boogert et al. (2015). Irradiation experiments of H_2O:CO ices performed by de Barros et al. (2022).

3. Data presented in Figs. 3 and 4 show that new species were formed during irradiation. Altogether, the new species identified are CO_2, HCO, C_2H_5OH, HCOOH, CH_4, H_2CO, and H_2O_2, and possible complex molecules ($HCOOCH_3$, CH_3CHO, CH_3COOH, and CH_3COCH_3) for the three samples. However, no significant difference is observed in the evolution of the CO_2, HCO, and C_2H_5OH column densities with projectile fluence. Further experimental investigations are needed to confirm the presence of the complex molecules.
4. The results presented here can help us understand how icy grain mantles in the ISM and CSE change due to ion irradiation. The chemical and sputtering yield modifications are dependent on the parameter E_0^n, and they are driven by the GCR distribution's intensity for energies $E < E_0$. Furthermore, the number of precursors in the sample increases these modification rates.

Acknowledgements. The CNPq 301868/ 2017-4 and 407938/ 2018-4, FINEP (0647/18), FAPERJ (E-26/210.965/ 2021, E-26/210.801/ 2021, E-26/245.307/ 2019 and E-26/241.202/ 2018) agencies are acknowledged for partial support. This study was financed in part by the Coordenação de Aperfeiçoamento de Pessoal de Nível Superior-Brazil (CAPES) FinanceCode001. We thank the GANIL and CIMAP personnel especially T. Been, C. Grygiel, and J. M. Ramillon for their essential support throughout the experiments.

References

Bennett, C. J., & Kaiser, R. I. 2007, ApJ, 660, 1289
Bennett, C. J., Jamieson, C. S., Osamura, Y., & Kaiser, R. I. 2005, ApJ, 624, 1097
Bergantini, A., Góbi, S., Abplanalp, M. J., & Kaiser, R. I. 2018, ApJ, 852, 70
Boduch, P., Dartois, E., de Barros, A. L. F., et al. 2015, J. Phys.: Conf. Ser., 629, 012008
Boogert, A. A., Gerakines, P. A., & Whittet, D. C. 2015, ARA&A, 53, 541
Bottinelli, S., Boogert, A. C. A., Bouwman, J., et al. 2010, ApJ, 718, 1100
Chiar, J. E., Pendleton, Y. J., Allamandola, L. J., et al. 2011, ApJ, 731, 9
Chuang, K.-J., Fedoseev, G., Ioppolo, S., van Dishoeck, E., & Linnartz, H. 2016, MNRAS, 455, 1702
Cummings, A., Stone, E., Heikkila, B., et al. 2016, ApJ, 831, 18
Dartois, E., Chabot, M., Barkach, T. I., et al. 2019, A&A, 627, A55
de Barros, A. L. F., Domaracka, A., Andrade, D. P. P., et al. 2011, MNRAS, 418, 1363
de Barros, A. L. F., da Silveira, E. F., Rothard, H., Langlinay, T., & Boduch, P. 2014, MNRAS, 443, 2733
de Barros, A. L. F., Mejía, C., Seperuelo Duarte, E., et al. 2022, MNRAS, 511, 2491
Duarte, E. S., Domaracka, A., Boduch, P., et al. 2010, A&A, 512, A71
Gerakines, P. A., Moore, M. H., & Hudson, R. L. 2001, J. Geophys. Res.: Planets, 106, 33381
Hudson, R., & Moore, M. 1999, Icarus, 140, 451
Ioppolo, S., Palumbo, M., Baratta, G., & Mennella, V. 2009, A&A, 493, 1017
Ivlev, A. V., Padovani, M., Galli, D., & Caselli, P. 2015, ApJ, 812, 135
Kaiser, R. I., Maity, S., & Jones, B. M. 2014, Phys. Chem. Chem. Phys., 16, 3399
Knez, C., Boogert, A. C. A., Pontoppidan, K. M., et al. 2005, ApJ, 635, L145
Maurin, D., Melot, F., & Taillet, R. 2014, A&A, 569, A32
McClure, M. K., Rocha, W. R. M., Pontoppidan, K. M., et al. 2023, Nat. Astron., 7, 431
Mejía, C., Bender, M., Severin, D., et al. 2015a, Nucl. Instrum. Methods Phys. Res. Sect. B , 365, 477
Mejía, C., de Barros, A., Duarte, E. S., et al. 2015b, Icarus, 250, 222
Mejía, C., de Barros, A. L. F., Rothard, H., Boduch, P., & da Silveira, E. F. 2020, ApJ, 894, 132
Mejía, C., De Barros, A., Rothard, H., Boduch, P., & Da Silveira, E. 2022, MNRAS, 514, 3789
Mejía Guamán, C. F., & Silveira, E. F. d. 2013, PhD thesis, PUC-Rio, Brazil
Mumma, M. J., & Charnley, S. B. 2011, ARA&A, 49, 471
Muñoz Caro, G. M., Ciaravella, A., Jiménez-Escobar, A., et al. 2019, ACS Earth Space Chem., 3, 2138
Padovani, M., Galli, D., Ivlev, A. V., Caselli, P., & Ferrara, A. 2018, A&A, 619, A144
Perotti, G., Rocha, W., Jørgensen, J., et al. 2020, A&A, 643, A48
Quirico, E., Bacmann, A., Wolters, C., et al. 2023, Icarus, 394, 115396
Shen, C., Greenberg, J., Schutte, W., & Van Dishoeck, E. 2004, A&A, 415, 203
Suhasaria, T., Baratta, G., Ioppolo, S., Zacharias, H., & Palumbo, M. E. 2017, A&A, 608, A12
Tanabashi, M., Hagiwara, K., Hikasa, K., et al. 2018, Phys. Rev. D, 98, 030001
Tielens, A. G. G. M. 2013, Rev. Modern Phys., 85, 1021
Whittet, D. C. B., Cook, A. M., Herbst, E., Chiar, J. E., & Shenoy, S. S. 2011, ApJ, 742, 28
Ziegler, J. F., Ziegler, M., & Biersack, J. 2010, Nucl. Instrum. Methods Phys. Res. Sect. B, 268, 1818